Differentiated Impacts of Urban Morphology on Land Surface Temperature across Local Climate Zones: Interaction and Seasonality

Geng Sun, Zikun Dong, Meng Cai, Ya Guo, Yang Chen, and Jie Chen, *Member, IEEE*

***Abstract*—Urban morphology is a key factor of land surface temperature (LST) variations. However, the heterogeneity of its impact mechanisms across spatial scales, seasons, and Local Climate Zones (LCZs) has not been fully explored. In this study, we first identify the optimal spatial scale at which urban morphological features exhibit the strongest explanatory power for LST. Based on this optimal scale, we systematically evaluate the relative contributions, marginal effects, and interaction mechanisms of impervious surfaces, vegetation, and water bodies on LST across LCZs and seasons. The results indicate that: the explanatory power of urban morphology on LST is highest at the 200-m scale; impervious surface metrics consistently contribute to higher LST across all LCZ types and seasons, whereas vegetation and water-related metrics generally exert cooling effects, especially during summer; and the interaction effects among morphological elements are significantly influenced by both seasonality and LCZ classification. This study uncovers the complex influence of multidimensional urban morphology on urban thermal environments under varying spatial and seasonal contexts. The findings can offer scientific insights for fine-grained and differentiated climate-adaptive urban planning and thermal environment management.**

***Index Terms*—Interaction effects, land surface temperature (LST), local climate zone (LCZ), seasonal variations, urban morphology.**

I. Introduction

THE urban heat island (UHI) effect, a typical byproduct of urbanization, has emerged as a critical issue in global urban climate change. Due to modifications of the urban surface, increased building density, and the reduction of green spaces, the land surface temperature (LST) in urban areas is generally higher than that in surrounding rural regions [1]. This phenomenon not only exacerbates urban energy consumption but also poses significant health risks to urban residents [2].

Urban morphology is considered one of the key drivers influencing LST variation [3]. Within urban built-up areas, impervious surfaces (e.g., buildings, roads, and paved grounds), water bodies, and vegetation are widely distributed. The morphological characteristics of these elements exert significant effects on LST [4], [5], [6], [7]. Impervious surfaces, due to their high thermal capacity and conductivity as well as the lack of evapotranspiration, serve as major sources of urban heat accumulation [8]. Moreover, the horizontal configuration and vertical structure of buildings can influence thermal circulation efficiency and surface wind speed [9]. Vegetation contributes to cooling not only through transpiration, which releases moisture and reduces local air temperature, but also by providing shade that limits direct solar radiation on surfaces [10]. Water bodies, through evaporation, can effectively delay temperature rise and heat release, making them an important means of regulating the urban microclimate [11]. Numerous previous studies have explored how urban morphological characteristics influence the UHI effect and LST, with a focus on the 2-D and 3-D configurations of impervious surfaces, vegetation, and water bodies [9], [12], [13]. These studies include land use or land cover (land use types and their spatial configuration) [13], [14], and building morphology (building height, building density, sky view factor (SVF), street width, and height-to-width ratio) [5], [12].

It is worth noting that the UHI effect is not uniformly distributed across urban areas. LST exhibits significant spatial heterogeneity within urban areas [7]. To understand urban thermal environments, lots of studies have focused on identifying the factors influencing LST at the microscales. Such fine-grained analysis provides valuable insights for urban planners to develop more precise and localized environmental regulation strategies [3], [15]. However, due to the absence of a unified standard for urban space typology, studies have reported inconsistent conclusions regarding the impact of urban morphology on thermal conditions [16]. Moreover, the limited regional applicability of these findings has constrained their broader application. To address these limitations, scholars have introduced a range of typological frameworks to describe urban space, including Urban Terrain Zones [17], Urban Climate Zones [18], and Urban

Received 9 July 2025; revised 5 September 2025; accepted 22 September 2025. Date of publication 29 September 2025; date of current version 27 October 2025. This work was supported in part by the Central South University Research Programme of Advanced Interdisciplinary Studies under Grant 2023QYJC033, in part by the National Natural Science Foundation of China under Grant 42371393, and in part by the National Key Research and Development Program of China under Grant 2024YFB3908602. *(Corresponding author: Jie Chen.)*

Geng Sun, Zikun Dong, Ya Guo, and Jie Chen are with the School of Geosciences and Info-Physics, Central South University, Changsha 410083, China (e-mail: cj2011@csu.edu.cn).

Meng Cai is with the School of Urban Design, Wuhan University, Wuhan 430072, China (e-mail: mengcai@whu.edu.cn).

Yang Chen is with the Department of Civil and Environmental Engineering, The Hong Kong Polytechnic University, Hong Kong SAR, China (e-mail: yangcee.chen@polyu.edu.hk).

This article has supplementary downloadable material available at https://doi.org/10.1109/JSTARS.2025.3615731, provided by the authors.

Digital Object Identifier 10.1109/JSTARS.2025.3615731

Functional Zones [19], which have subsequently been applied in UHI studies. Among these classification systems, the Local Climate Zone (LCZ) framework integrates both morphological and functional characteristics of urban landscapes, providing a high degree of standardization and comparability [20]. These features make it suitable for cross-city and global-scale urban thermal environment studies.

The LCZ system categorizes urban surfaces into 17 standardized climate zones—10 built types and 7 natural types. Each zone exhibits similar physical attributes, such as building height, surface materials, and vegetation cover, making the LCZ system particularly suited for explaining thermal environment variations at the microscales. Compared to traditional land use classifications, the LCZ system demonstrates greater explanatory power in revealing the spatial heterogeneity mechanisms of LST [21], [22]. Previous studies have primarily examined the spatiotemporal relationships between LCZ and LST or UHI [22], [23]. From the temporal perspective, several studies have explored diurnal and seasonal variations of LST across different LCZ types [21], [24], [25], [26]. From the spatial perspective, some studies have compared LST differences among LCZ types across various latitudes and climatic regions [6] or examined the nonstationary spatial influence of LCZ distribution within cities on LST patterns [27].

Significant differences in urban morphology exist among LCZ types, which may influence the mechanisms of heat accumulation and transfer [28]. Consequently, numerous studies have analyzed the influence of 2-D and 3-D morphological metrics of impervious surfaces, water bodies, and vegetation on LST across LCZ types [29], [30], [31], [32]. For instance, Feng et al. [33] analyzed Landsat-derived LST in Zhengzhou, China, and demonstrated that landscape configuration metrics explained the largest share of LST variation within built-type LCZs, whereas moisture and brightness indices dominated in nonbuilt LCZs. In Eastern Europe, a long-term study (1984–2022) of six Romanian cities revealed that industrial and compact built LCZs consistently corresponded to hot spots, whereas forest and water LCZs acted as persistent cool islands [34]. Comparative analyses in arid cities such as Phoenix and Tucson, USA, further highlighted the strong warming contribution of barren land and impervious LCZs, contrasted with significant cooling effects from vegetated and water-based LCZs [35]. Similarly, a study in Poland showed that increases in open midrise LCZs and impervious density were linearly associated with higher LST, with shifts from natural to built LCZs leading to an average rise of 1.19 °C [36]. These studies highlight the distinct thermal environmental mechanisms across LCZs and reveal that morphological metrics—such as SVF, building density, and green cover—exhibit nonlinear and nonstationary thermal response pathways within LCZs [5], [37], [38]. Neglecting these differences may introduce biases in understanding how multidimensional urban morphology influences the UHI effect, impairing accurate assessments of urban thermal environments. Therefore, studying the mechanisms and differential impacts of multidimensional urban morphology across LCZ types is critical for comprehending the complexity and spatial heterogeneity of the UHI effect.

Nevertheless, most previous studies investigating the influence of urban morphology within LCZs have primarily relied on correlation-based analyses. Commonly used methods include traditional regression models, such as linear regression [39], spatial regression [40], as well as machine learning models such as random forest [41], Geodetector [42], and eXtreme Gradient Boosting (XGBoost) models [43]. Existing research has predominantly focused on the independent effects of single variables, with limited attention to the interaction mechanisms among urban morphological metrics. In fact, impervious surfaces, water bodies, and vegetation elements often coexist within urban built-up areas and may exhibit complex interactions. For instance, in areas with a high proportion of impervious surfaces, the cooling effect of relatively abundant vegetation cover can be suppressed. Conversely, regions with an ideal arrangement of water bodies and green spaces may experience enhanced cooling effects due to their interaction [10]. Therefore, exploring the interactive mechanisms among impervious surfaces, vegetation, and water bodies under different morphological contexts is crucial for a comprehensive understanding of the urban thermal environment.

Besides, although models such as XGBoost demonstrate excellent predictive performance, their nature as black-box models limits interpretability and hinders deep understanding of the contributions of individual features [44]. To address the black-box problem in machine learning, Lundberg and Lee proposed the SHapley Additive exPlanations (SHAP) method [45]. SHAP quantifies the marginal contribution of each variable to the prediction outcome, distinguishes positive and negative feature impacts, and provides interpretability at both global and local levels [5]. Coupling SHAP with the XGBoost model not only enhances model interpretability but also systematically reveals the interaction pathways among urban morphological variables, thereby supporting understanding their complex thermal effect mechanisms.

Furthermore, previous investigations into the interactions of urban morphology have typically examined the effects of different urban morphology on LST using a single season and predefined spatial scales. However, the influence of various land cover types on LST varies across both seasonal and spatial scales. On one hand, the driving mechanisms of LST exhibit significant seasonal dynamics, as seasonal variations affect the thermal regulation capacities of different elements. For example, vegetation transpiration is stronger and cooling effects are more prominent in summer, whereas in winter these effects may diminish due to leaf shedding or reduced evapotranspiration [37]. Consistently, Xiang et al. [46] demonstrated that the normalized difference vegetation index (NDVI) exerts a cooling effect during summer and transitional seasons (spring and autumn), but shifts to a warming effect in winter, a finding that aligns with the conclusions of [40]. On the other hand, the functional mechanisms of morphological elements vary across spatial scales [32]. A growing body of recent studies confirms the critical role of scale selection. For instance, Xu et al. [47], analyzing 3-D urban form metrics in Shanghai, found that correlations between morphology and LST were strongest at $\sim$1050

m, underscoring how scale choices can significantly shape conclusions on urban thermal environments. Similarly, Ge et al. [48] demonstrated in the Chang-Zhu-Tan urban agglomeration that integrating 2-D landscape and 3-D form indicators within the LCZ framework reveals LST variation mechanisms, with the optimal spatial scale differing by season. From a European context, Pappaccogli et al. [49], using ECOSTRESS data, highlighted scale-dependent effects in Lecce and Milan, showing that finer spatial scales of a few hundred meters better captured local thermal contrasts among LCZs. Therefore, it is essential to identify the optimal spatial scale—the scale at which urban morphological features exhibit the strongest influence for LST variations. This optimal scale serves as a robust foundation for subsequent analyses. At this scale, we further examine seasonal variations and differences across LCZ types to elucidate the nuanced influences and interactions of urban morphology on LST.

In summary, this study aims to analyze the scale effects and interaction mechanisms of urban morphological features on LST from the perspective of LCZs, with a particular focus on their cross-factor interactions and seasonal differences. In this study, first, we calculated the urban morphology metrics of impervious surfaces, vegetation, and water bodies. Second, we assessed the scale effects of morphological metrics on LST to determine the optimal scale and identified LCZs at the optimal scale. Finally, we employ the XGBoost regression model coupled with the SHAP method to examine the relationships between urban morphological characteristics and LST. These analyses aim to answer the following three questions.

1) At which spatial scale do the morphological metrics of impervious surfaces, vegetation, and water bodies exert the greatest influence on LST?
2) How do the interactive effects of these morphological elements on LST across LCZ types?
3) What are the seasonal differences in the interaction effects of impervious surfaces, vegetation, and water bodies on LST?

II. Study Area and Data

A. Study Area

Changsha is located between 111°53' E and 114°15' E and 27°51' N and 28°41' N, spanning both sides of the Xiangjiang River. The topography of Changsha is characterized by higher elevations in the northeast and northwest, whereas the central part of the city features a relatively flat terrain with lower elevations. Changsha falls within the subtropical monsoon climate region, experiencing short spring and fall seasons, accompanied by long summers and winters. The city experiences approximately 30 days per year with temperatures exceeding 35 °C. According to the Seventh National Population Census, the urbanization rate of Changsha has reached 82.60%, surpassing the urbanization level of developed countries (80%). The rapid urbanization of Changsha has resulted in a substantial increase in population and building density, exacerbating the thermal environment effect. Therefore, understanding the specific driving mechanisms of the LST across different LCZs in Changsha is crucial for improving the urban thermal environment.

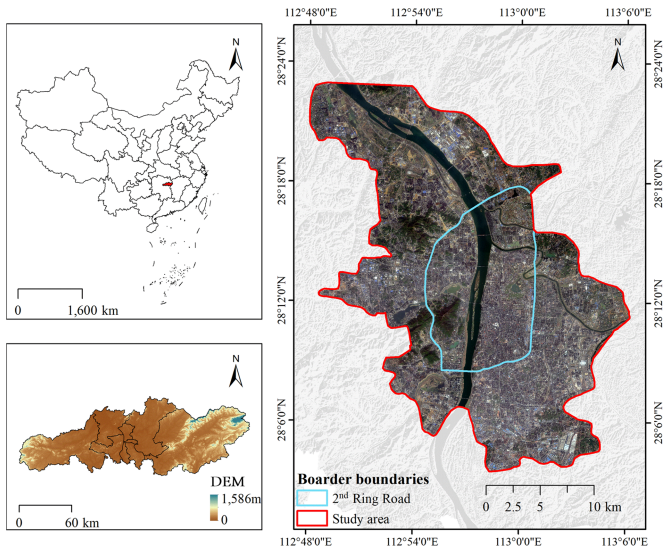

Fig. 1. Study area.

TABLE I
Description of the Data Used in This Study

Data Type	Time	Data Sources	Spatial Resolution	Application
Landsat Collection 2 Level-2	2022-1-13, 2022-3-2, 2022-8-9, 2022-10-12	USGS (https://earthexplorer.usgs.gov/)	30 m	LST
High Resolution Satellite Images (HRSI)	2022	Tianditu(www.tianditu.gov.cn)	1 m	Morphology Metrics & LCZ
Building Footprint	2022	Amap(https://lbs.amap.com/)	-	Morphology Metrics
Vegetation Canopy Height	2020	[50]	10 m	Morphology Metrics

As shown in Fig. 1, the study area includes the 2nd Ring Road of Changsha and the surrounding built-up areas, covering a total area of 577.36 km^2. Within this region, the buildings within the 2nd Ring Road primarily consist of dense midrise and high-rise structures. In contrast, outside the 2nd Ring Road, there is a greater diversity of building forms, including low-density low-rise buildings and factories. This diverse urban morphology within the study area provides an ideal context to investigate the influence of urban morphology characteristics on the local thermal environment.

B. Data and Preprocessing

To analyze the impact of urban morphology on LST, this study collected a dataset that encompassed spatial morphology characteristics, including remote sensing images, building vectors, and canopy height. Table I provides an overview of the data sources utilized in the analysis.

Band 10 of the Landsat Collection 2 Level-2 product, known as the Surface Temperature Band (STB10), is used to derive LST. To calculate the LST for the spring, summer, fall, and winter seasons in Changsha, we obtained Landsat imagery from March 2, 2022, August 9, 2022, October 12, 2022, and January 13, 2022, respectively. The LST in Kelvin (LST_k) can be calculated from STB10 using

$$LST_k = ST_{B10} \times 0.00341802 + 149 \quad (1)$$

where the LST_k is obtained by linearly scaling STB10 using a multiplicative scaling factor of 0.00341802 and an additive offset of 149. The conversion from Kelvin to degrees Celsius is performed using

$$LST = LST_k - 273.15. \quad (2)$$

HRSI from 2022 were used to classify land cover in the study area. Specifically, an interpretation model provided by the AI Earth platform was employed to identify eight land cover types: cropland, forest, grassland, buildings, roads, structures, artificial excavation sites, bare land, and water bodies. Based on the classification results, this study reclassified the land cover types using the reclassification function in ArcGIS into 4 major categories: vegetation (cropland, forest, and grassland), impervious surfaces (buildings, roads, and structures), water bodies, and others (bare land, artificial excavation sites). The overall accuracy of this land cover classification, compared to the labeled ground truth, was 78.1%. Besides, the building footprint data and vegetation canopy height data offer the 3-D information of imperious surfaces and vegetation.

III. Method

A. Study Framework

Our research framework is shown in Fig. 2. It consists of three main steps.

1) Data Collection and Metrics Calculation.
2) Optimal scale Determination.
3) The Impacts of Urban Morphology on LST across LCZ Types and Seasons.

First, based on land cover classification results derived from HRSIs, building footprint data, and canopy height data, we calculated 2-D and 3-D morphological metrics for impervious surfaces, vegetation, and water bodies across multiple spatial scales. Second, to determine the optimal scale at which urban morphological variables most strongly influence LST, we applied the Geographically Optimal Zones-based Heterogeneity (GOZH) method [51]. We classified the LCZ of each analysis unit using a deep learning algorithm applied to HRSI at the identified optimal scale. Finally, for different seasons and LCZ types, we employed the XGBoost algorithm to model the relationship between urban morphological metrics and LST. We further incorporated the SHAP method to quantify the contribution and interaction effects and seasonal variations of metrics. This integrated approach enables a comprehensive understanding of the complex relationships between urban morphology and LST.

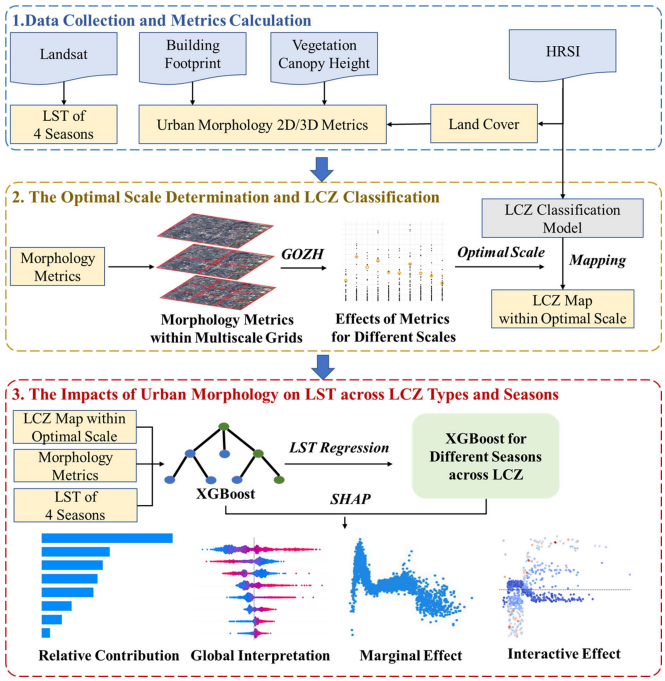

Fig. 2. Research framework. The framework includes: 1. Data collection and metrics calculation, 2. The optimal scale determination and LCZ classification, and 3. The impacts of urban morphology on LST across LCZ types and seasons.

B. Urban Morphological Metrics

1) Metrics Definition: The urban morphological metrics used in this study are shown in Table II. The 2-D metrics include patch cohesion index (COHESION), disjunct core area density (DCAD), landscape division index (DIVISION), edge density (ED), mean fractal dimension index (FRACMN), largest patch index (LPI), mean perimeter-area ratio (PARAMN), percentage of landscape (PLAND), splitting index (SPLIT), mean architecture projection area (MAPA), and building surface fraction (BSF). In addition to the 2-D metrics, this study also considered the 3-D morphological characteristics of buildings and vegetation. The 3-D metrics of impervious include: mean building height (MBH), standard deviation of building height (BHSD), floor area ratio (FAR), SVF, and average volume (V).

The 3-D metrics of vegetation include mean canopy height (MCH) and standard deviation of canopy height (CHSD). This comprehensive set of 2-D/3-D morphology metrics provides an analytical framework to investigate the influence of impervious surfaces, vegetation, and water bodies morphological metrics on LST within the study area.

2) Metrics Calculation: Considering the effect of scale, it is essential to determine the appropriate analysis scale before investigating the influence mechanisms of urban morphology on LST. To this end, the study area was first divided into grid cells of varying sizes ranging from 100 to 1000 m to generate analysis units at different spatial scales. Subsequently, based on land cover classification results from HRSI, building footprint data, and vegetation canopy height data, we calculated the 2-D and 3-D morphological metrics of impervious surfaces, vegetation, and water bodies for each analysis unit at multiple scales.

TABLE II
MORPHOLOGICAL METRICS USED IN THIS STUDY

Metrics	Formula	Description	Variable name
MBH	$MBH = \frac{\sum_{i=1}^{n} BH_i}{n_b}$	The average height of building. BH_i is the height of the building i. n_b is the number of buildings.	(1) IM_MBH
MCH	$MCH = \frac{\sum_{i=1}^{n} CH_i}{n_c}$	The average height of vegetation. CH_i is the height of the vegetation pixel i. n_c is the number of vegetation pixels.	(2) VE_MCH
BHSD	$BHSD = \sqrt{\frac{\sum_{i=1}^{n}(BH_i - MBH)^2}{n_b}}$	Standard deviation of the building height.	(3) IM_BHSD
CHSD	$CHSD = \sqrt{\frac{\sum_{i=1}^{n}(CH_i - MCH)^2}{n_c}}$	Standard deviation of the vegetation height.	(4) VE_CHSD
FAR	$FAR = \frac{\sum_{i=1}^{n}(t \times F)}{A}$	The ratio of the total built-up area within a patch to the total size of patch. t is the number of floors on a single building. F is the land area of building. A is the landscape area.	(5) IM_FAR
MAPA	$MAPA = \frac{TAPA}{n_b}$	The mean area of architecture projected vertically to floor. $TAPA$ is the total architecture projection area.	(6) IM_MAPA
BSF	$BSF = \frac{\sum_{i=1}^{n} BS_i}{A}$	Percentage of the areas of all patches of buildings to total landscape area. BS_i is the area of the building i.	(7) IM_BSF
SVF	$SVF = 1 - \sum_{i=1}^{n} \sin^2\beta_i \left(\frac{\alpha_i}{360°}\right)$	The ratio of visible sky area to the hemisphere. α_i and β_i are the elevation and azimuth angles of the angle element i, respectively.	(8) IM_SVF
V	$V = \frac{\sum_{i=1}^{n} V_i}{n_b}$	V_i is the building volume of the building i.	(9) IM_V
AI	$AI = \left[\frac{g_{ii}}{max \rightarrow g_{ii}}\right](100)$	The number of like adjacencies involving the corresponding class, divided by the maximum possible number. g_{ii} is the number of joins between pixels of type i.	(10) IM_AI (11) VE_AI (12) WA_AI
COHESION	$COHESION = \left[1 - \frac{\sum_{j=1}^{n} p_{ij}}{\sum_{j=1}^{n} p_{ij}\sqrt{a_{ij}}}\right] \cdot \left[1 - \frac{1}{\sqrt{Z}}\right]^{-1} \cdot (100)$	The connectivity of the same type within the total landscape area. p_{ij} is the perimeter of j-th patch of type i. a_{ij} is the area of jth patch of type i. Z is the total numer of pixels within the landscape area.	(13) IM_COHESION (14) VE_COHESION (15) WA_COHESION
DCAD	$DCAD = \frac{\sum_{j=1}^{n} n_{ij}^{c}}{A}$	The mean of disjunct core areas in the landscape area. n_{ij}^{c} is the disjunct core area of j-th patch of type i.	(16) IM_DCAD (17) VE_DCAD (18) WA_DCAD
DIVISION	$DIVISION = \left[1 - \sum_{i=1}^{m}\sum_{j=1}^{n}\left(\frac{a_{ij}}{A}\right)^2\right]$	The probability that two random pixels in a landscape area belong to different types	(19) IM_DIVISION (20) VE_DIVISION (21) WA_DIVISION
ED	$ED = \frac{\sum_{k=1}^{m} e_{ik}}{A}(10000)$	Total lengths of all edge segments involving the corresponding type divided by the total landscape area. e_{ik} is the length of the kth patch of type i.	(22) IM_ED (23) VE_ED (24) WA_ED
FRACMN	$FRACMN = \frac{2\,ln(0.25p_{ij})}{n\,ln\,a_{ij}}$	The degree of complexity of the corresponding type.	(25) IM_FRACMN (26) VE_FRACMN (27) WA_FRACMN
LPI	$LPI = \frac{\max_{j=1}^{n}(a_{ij})}{A}(100)$	Percentage of area of the patch with the largest area of the type i to the total landscape area.	(28) IM_LPI (29) VE_LPI (30) WA_LPI
PARAMN	$PARAMN = \frac{p_{ij}}{na_{ij}}$	The ratio of the patch perimeter to area.	(31) IM_PARAMN (32) VE_PARAMN (33) WA_PARAMN
PLAND	$PLAND = P_i = \frac{\sum_{j=1}^{n} a_{ij}}{A}(100)$	Percentage of the areas of all patches of the corresponding patch type to the total landscape area.	(34) IM_PLAND (35) VE_PLAND (36) WA_PLAND
SPLIT	$SPLIT = \frac{A^2}{\sum_{j=1}^{n} {a_{ij}}^2}$	The degree of fragmentation of the corresponding type.	(37) IM_SPLIT (38) VE_SPLIT (39) WA_SPLIT

Note: In the following content, abbreviations like IM_PLAND, VE_PLAND, and WA_PLAND mean the percentage of landscape of impervious surface, vegetation, and water body, respectively.

The 2-D metrics were obtained from land use results by Fragstats 4.2 [52], including COHESION, DCAD, DIVISION, ED, FRACMN, LPI, PARAMN, PLAND, and SPLIT of impervious surfaces, vegetation, and water bodies. SVF was calculated using SAGA GIS [53]. The remaining morphology metrics, including MAPA, BSF, MBH, BHSD, FAR, V, MCH, and CHSD, were calculated using a Python program on building vectors and vegetation canopy height data. Since the calculation of water-related morphological indicators (e.g., WA_PLAND) is only meaningful in analytical units that contain water bodies, this study restricted the computation of these metrics to waterfront areas. The impervious surface metrics and vegetation were calculated on all areas. In this study, waterfront areas are defined as grid cells that contain water bodies. These grid cells are identified based on the presence of significant water features such as rivers and lakes within the boundaries of each grid cell.

C. Optimal Scale Determination and LCZ Classification

1) Determining the Optimal Scale: The key to selecting the optimal analysis scale is assessing the explanatory power of

morphological metrics on LST. Existing multiscale studies include correlation and spatial autocorrelation analysis [54], scale selection based on the predictive power of metrics [55], vegetation landscape index optimization based on response curves [56], variance analysis-based scale testing [57], etc. Given that the spatial heterogeneity of morphological features at different scales may affect their explanatory power for LST, a method capable of comprehensively evaluating multiscale metric heterogeneity is required. Therefore, this study adopts the GOZH method [51], which evaluates spatial heterogeneity across multiple scales and identifies the optimal scale by maximizing the Optimal Power of Determinant (OPD).

In practice, we employed the GOZH method to calculate the OPD (represented by Ω) based on the morphology metrics and LST of each grid cell at multiscales (from 100 to 1000 m). The Ω of each metric at each season and local scale were calculated with

$$\Omega = \text{maxPD} = 1 - \frac{\text{minSSW}_{X,D}}{\text{SST}} \tag{3}$$

where X is the explanatory variable, D is the stratified explanatory variable, SSW is the sum of squares of D recorded by the explanatory variable X, and SST is the sum of squares of LST in the entire study area. For each scale, Ω values were obtained for all metrics over the four dates, and the optimal scale was determined based on the 90% quantile of the Ω values [58].

2) LCZ Classification: To generate the LCZ maps of the study area, an improved labeling process based on the So2Sat LCZ42 dataset was implemented [59]. Before labeling, a consensus on the labeling standards was established by studying the criteria for classifying LCZ types. The LCZ samples are listed in Section A of Supplementary. Compared to medium resolution remote sensing data such as Landsat and Sentinel, HRSI can provide detailed features of ground objects and accurately map urban landscapes [60], [61]. Therefore, this study uses the HRSIs of Tianditu for LCZ classification. Initially, the Tianditu images within homogeneous areas were cropped to the identified optimal scale. These cropped images were then used to annotate the samples. Subsequently, three volunteers with expertise in remote sensing conducted visual inspections of all the labeled samples. Only the samples that received a majority vote were selected, ensuring the retention of accurate LCZ labels. Finally, to ensure the precision of the deep learning-based LCZ supervised classification, the balance of samples between natural and built-up areas in the dataset was considered. Specifically, the number of samples for each natural class was controlled so that it did not exceed the class with the highest number of built-up area samples. Besides, considering the absence of lightweight low-rise buildings (LCZ 7), nine building types comprising LCZs 1–6 and LCZs 8–10, along with seven natural land cover types (LCZs A-G), were identified.

ResNet-50 was selected as the LCZ classification method due to its effectiveness in addressing the issue of gradient vanishing through the incorporation of residual connections [62]. Additionally, ResNet-50 is a widely adopted backbone in scene-level LCZ classification methods, as demonstrated by the work of Huang et al. [63]. Approximately 1100 samples were selected and randomly divided into a training set with four-fifths of the samples and a testing set with one-fifth of the samples. The ResNet-50 model was trained using the PyTorch deep learning platform, with 200 iterations. Several metrics were employed to assess the accuracy of the classification, including overall accuracy (OA) and urban area overall accuracy (OA_U) [64]. The formulas used for assessing LCZ classification are listed in Section A of Supplementary.

D. Impacts of Urban Morphology on LST

1) LST Regression Based on XGBoost: In this study, the XGBoost regression model is employed to reveal the nonlinear relationships between the urban morphological metrics of impervious surfaces, vegetation, and water bodies (as the feature variables) and LST (as the response variable) while incorporating LCZ types and seasons (as the control variables). We trained separate regression models for each built LCZ type and each season in Changsha to explore the influence of morphology metrics on LST under different morphology contexts and seasonal conditions.

In practice, the model was implemented using the "XGBoost" library in Python, with tenfold cross-validation and grid search employed to determine the optimal combination of hyperparameters [65]. Following the parameter settings adapted from previous studies [6], [66], we configured the XGBoost model as follows: the number of estimators ranged from 1000 to 4000 in increments of 100. The learning rate was fixed at 0.005. The maximum depth of the trees was tested between 4 and 6 with a step size of 4. The minimum sum of instance weights varied between 1 and 5 in steps of 2. The subsample ratio for individual trees was set at 0.7, whereas the column sampling ratio per tree was set at 0.6 and 0.8. The regularization parameter gamma ranged from 0 to 0.3 with an increment of 0.1. A 3:1 split was applied to divide the dataset into training and validation subsets. Model accuracy was assessed using the coefficient of determination (R^2) and mean absolute error (MAE). R^2 quantifies the proportion of variance in the dependent variable explained by the model, whereas MAE calculates the mean magnitude of the errors between predicted and actual observations.

2) Interpretability Analysis Based on SHAP: SHAP quantifies the marginal contribution of each feature across different feature combinations, offering a consistent and theoretically sound approach to model explanation. As an additive attribution framework, SHAP treats features as cooperative players and assigns each one a SHAP value for every prediction, indicating how much it increases or decreases the predicted outcome [67]. This makes SHAP a valuable tool for uncovering the relative influence of urban morphological metrics on variations in LST. Compared to traditional models that typically provide only global feature importance, one major advantage of SHAP lies in its ability to offer both global and local (instance-level) interpretability. It not only identifies the direction (positive or negative) of each feature's impact but also captures interactions among features [68].

Therefore, we employed the "SHAP" library in Python to interpret features based on the XGBoost model in this study. This approach allows us to obtain global feature influence and further analyze the marginal and interaction effects of the variables, thereby enabling a deeper understanding of the nonlinear relationships between urban morphology and LST. The SHAP values were calculated following the definition proposed in [45].

$$\phi_i = \sum_{S \subseteq M \setminus \{i\}} \frac{|S|!\,(|M|-|S|-1)!}{|M|!} \left(f_{S\cup\{i\}}\left(x_{S\cup\{i\}}\right) - f_S\left(x_S\right)\right) \tag{4}$$

where Φ_i is the contribution of the variable i, the M denotes the set of all input variables, f represents the prediction function model, S represents the set of all input variables excluding i, and x represents the values' vector at a certain instance. The positive SHAP value means the warming effect of potential drivers on LST, whereas the negative SHAP value represents the cooling effect.

To explain the interaction effects between highly correlated features, we calculated SHAP interaction values. This method quantifies the portion of the combined effect of two specific features that cannot be explained by the sum of their individual effects, thereby capturing their interaction. Theoretically, the SHAP interaction value is derived by replacing the external subset of variables S and computing the weighted average of $\delta_{i,j}(S)$, which reflects the interaction between i and j features. Specifically, $\delta_{i,j}(S)$represents the joint contribution of two features, subtracting the sum of their marginal contributions under the same background feature set. The detailed calculation method is shown as follows:

$$\begin{aligned} \phi_{i,j} &= \sum_{S \subseteq M \setminus \{i,j\}} \frac{|S|!\,(|M|-|S|-2)!}{2\,(|M|-1)!} \delta_{i,j}\left(S\right) \\ \delta_{i,j}\left(S\right) &= f_{S\cup\{i,j}\left(x_{S\cup\{i,j\}}\right) - f_{S\cup\{i\}}\left(x_{S\cup\{i\}}\right) \\ &\quad - f_{S\cup\{j\}}\left(x_{S\cup\{j\}}\right) + f_S\left(x_S\right) \end{aligned} \tag{5}$$

where $\phi_{i,j}$ is the interaction of the variable i and j, the M denotes the set of all input variables, f represents the prediction function model, S represents the set of all input variables excluding i, and x represents the values' vector a certain instance.

In this study, we employed SHAP summary plots to visualize the SHAP values across all samples, providing an overall perspective of the influence each feature has on LST. Features are ranked according to their importance, indicating their contribution to the model's predictions and general effect patterns. To further elucidate the mechanisms behind specific variables, dependence plots were used to display the distribution of SHAP values for individual features [66]. Moreover, to gain a deeper understanding of the interactions among features, we combined the use of SHAP values with SHAP interaction values. These interaction values capture variations in predictions arising from the synergistic effects between pairs of features. Compared to relying solely on individual feature SHAP values, dependence plots based on interaction values reveal underlying nonlinear relationships and complex interaction mechanisms between variables.

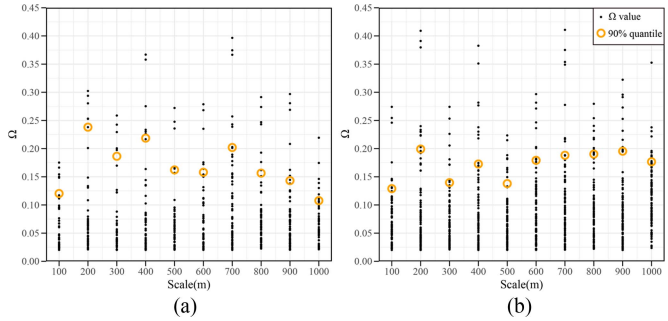

Fig. 3. Spatial scale effects and spatial scale selection results for (a) whole study area and (b) waterfront area.

IV. Result

A. Optimal Scale

Fig. 3 shows the distribution of Ω values across ten different spatial scales. By examining the variation patterns of Ω in each plot, it is evident that morphological features explain LST more reliably at smaller scales. This is likely because finer spatial details of land cover types are more accurately captured at smaller scales. As the scale increases, these details become increasingly "smoothed out," leading to a reduction in the explanatory power of morphological metrics on LST. Analyzing the 90th percentile of Ω values at each scale reveals a peak at the 200-m scale, indicating that at this scale, the explanatory strength and significance of morphological features on LST are the highest within the study area. Therefore, from the perspective of morphology's explanatory power on the thermal environment, 200 m is the optimal scale.

B. LCZ Classification Results

The LCZ classification at the 200-m scale is shown in Fig. 4. The LCZ classification achieved an OA of 80.54%, and the OAU reaches 75.91% for the urban classes. The built types in the study area include LCZ 1, LCZ 2, LCZ 3, LCZ 4, LCZ 5, LCZ 6, LCZ 8, LCZ 9, and LCZ 10. The main built-up areas are classified as LCZ5, covering 18.7% of the study area. LCZB and LCZG cover larger proportions at 16.56% and 8.8%, respectively.

C. Impacts of Urban Morphology on LST Across LCZ Types and Seasons

1) Relative Contribution of Metrics: The XGBoost regression results indicate that the models' R^2 values are all above 0.6, and MAE values remain below 2 across built LCZ types and seasons (see Supplementary Table I). In Fig. 5, we present the top ten metrics with the highest absolute SHAP values affecting LST across built LCZ types for each season. The results reveal significant differences in the impact of urban morphological metrics on LST. Morphological metrics of impervious surfaces, vegetation, and water bodies influence LST in all LCZ types and seasons, with the contribution of impervious surface metrics being particularly prominent.

Specifically, among the impervious surface metrics, IM_MBH is the most influential factor in spring (ranking first in 6 LCZ types) and winter (ranking first in nine LCZ

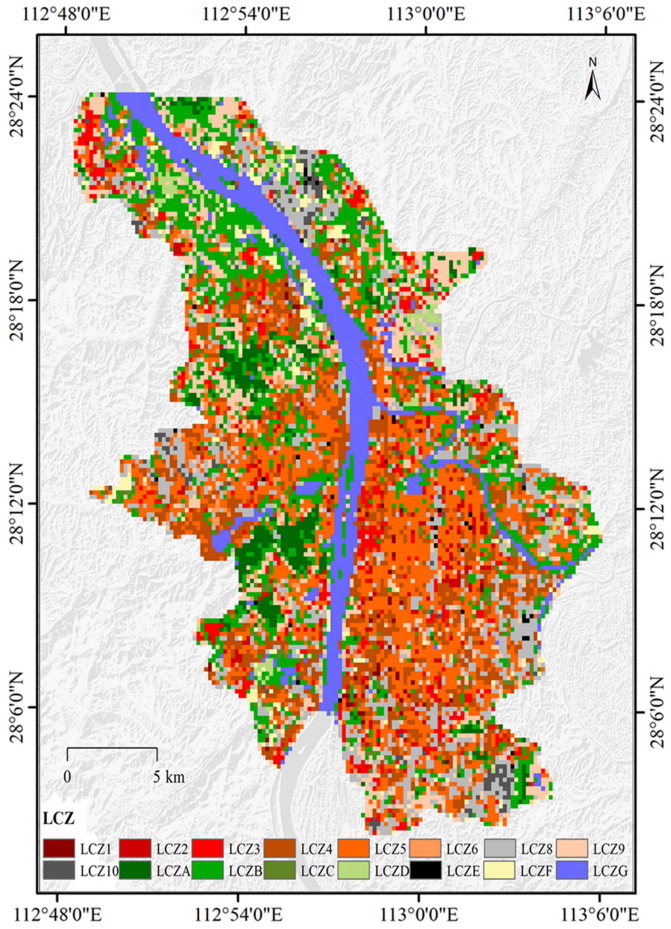

Fig. 4. Spatial distribution of LCZ at 200 m.

types). IM_PLAND dominates in summer (ranking first in eight LCZ types) and fall (ranking first in five LCZ types). Other impervious surface metrics, such as IM_MAPA and IM_BSF, also rank highly in the SHAP values across LCZ types and seasons, further highlighting the dominant role of impervious surface morphology in affecting LST. Regarding vegetation metrics, VE_CHSD appears in the top ten for seven LCZ types during spring and winter, VE_MCH ranks in the top ten for nine LCZ types in summer, and VE_ED is among the top ten in six LCZ types in fall. For water-related metrics, WA_PLAND shows high influence across seven LCZ types in spring, six in summer, and seven in winter, whereas WA_AI ranks within the top ten for nine LCZ types in fall.

By comparing the SHAP values across seasons, it can also be found that SHAP values are generally higher in summer and lower in winter. This indicates that LST is more susceptible to the influence of urban spatial morphology in summer. Additionally, different LCZ types exhibit varying responses to morphological metrics. For instance, in summer, IM_PLAND ranks first in LCZ 1, LCZ 2, LCZ 4, LCZ 5, LCZ 6, LCZ 8, LCZ 9, and LCZ 10, but only ranks third in LCZ 3. The ranking of the vegetation metric VE_MCH fluctuates between 5th and 8th across different LCZs. The water morphology metric WA_PLAND is most influential in LCZ 2, LCZ 3, LCZ 5, LCZ 8, LCZ 9, and LCZ 10, but does not appear in the top ten for LCZ 1, LCZ 4, and LCZ 6. These findings highlight the complex nonlinear relationships between urban morphological metrics and LST, with their influence mechanisms modulated by both morphological context and seasonal variations.

2) Global Interpretation of Metrics Relative Contribution of Metrics: The results shown in Fig. 6 indicate that different urban morphological metrics have significant positive or negative effects on LST. Specifically, impervious surface metrics such as IM_PLAND, IM_MAPA, IM_BSF, and IM_AI exhibit significant positive correlations (warming effect) with LST, suggesting that increases in these factors generally exacerbate urban heat conditions. Conversely, IM_MBH and several water body and vegetation-related metrics, including WA_PLAND, WA_AI, WA_DCAD, VE_PLAND, VE_ED, VE_CHSD, and VE_MCH, show significant negative correlations (cooling effect) with LST. This highlights the critical role that the spatial morphology of water bodies and vegetation plays in mitigating the urban heat island effect.

3) Marginal Effect of Metrics: We analyzed the marginal effects of key metrics on LST across different seasons and LCZ types. Specifically, based on the results of relative contribution, six important metrics were selected from impervious surfaces (IM_MBH, IM_PLAND), vegetation (VE_MCH, VE_PLAND), and water bodies (WA_AI, WA_PLAND). Seasonal variations of these metrics are reflected in the range of SHAP values, with summer showing a generally wider SHAP value range, indicating a stronger impact of these metrics on LST during summer. Differences in the metrics among LCZ types are observed in the direction and magnitude of the effects of the same metric values on LST.

Specifically, as the results shown in Fig. 7, for impervious surface morphology, in LCZ 2 during spring and winter, when IM_MBH$<$10 m, it has a warming effect on LST. In other seasons and LCZ types, IM_MBH$<$8m generally exhibit a cooling effect on LST, which shifts to a warming influence once IM_MBH exceeds 8 m. When 10 m$<$IM_MBH$<$18 m, it positively contributes to increased LST. As IM_MBH surpasses 18 m, its cooling effect on LST gradually strengthens. However, when IM_MBH$>$25 m, the cooling effect on LST becomes unstable. Regarding IM_PLAND, it typically exerts a cooling effect on LST when below 60%, but once it exceeds 60%, the effect turns warming, with a more prominent impact during summer (see Fig. II in Supplementary). For vegetation morphology, VE_MCH usually causes a weak warming effect on LST when below 3 m, but switches to a cooling effect as it exceeds 3 m (see Fig. III in Supplementary). VE_PLAND generally shows a cooling effect when above 8% (see Fig. IV in Supplementary). As for water body morphology, WA_PLAND tends to have a cooling effect when above 5% (see Fig. V in Supplementary). WA_AI demonstrates a significant cooling effect once it surpasses 96 (see Fig. VI in Supplementary).

4) Interactive Effect of Metrics: Through analyzing the interaction effects among the morphological metrics, it can be found that significant interactions between IM_MBH and WA_PLAND (see Fig. VII in Supplementary), as well as between WA_PLAND and VE_DCAD (see Fig. VIII in Supplementary). Moreover, these interaction values varied

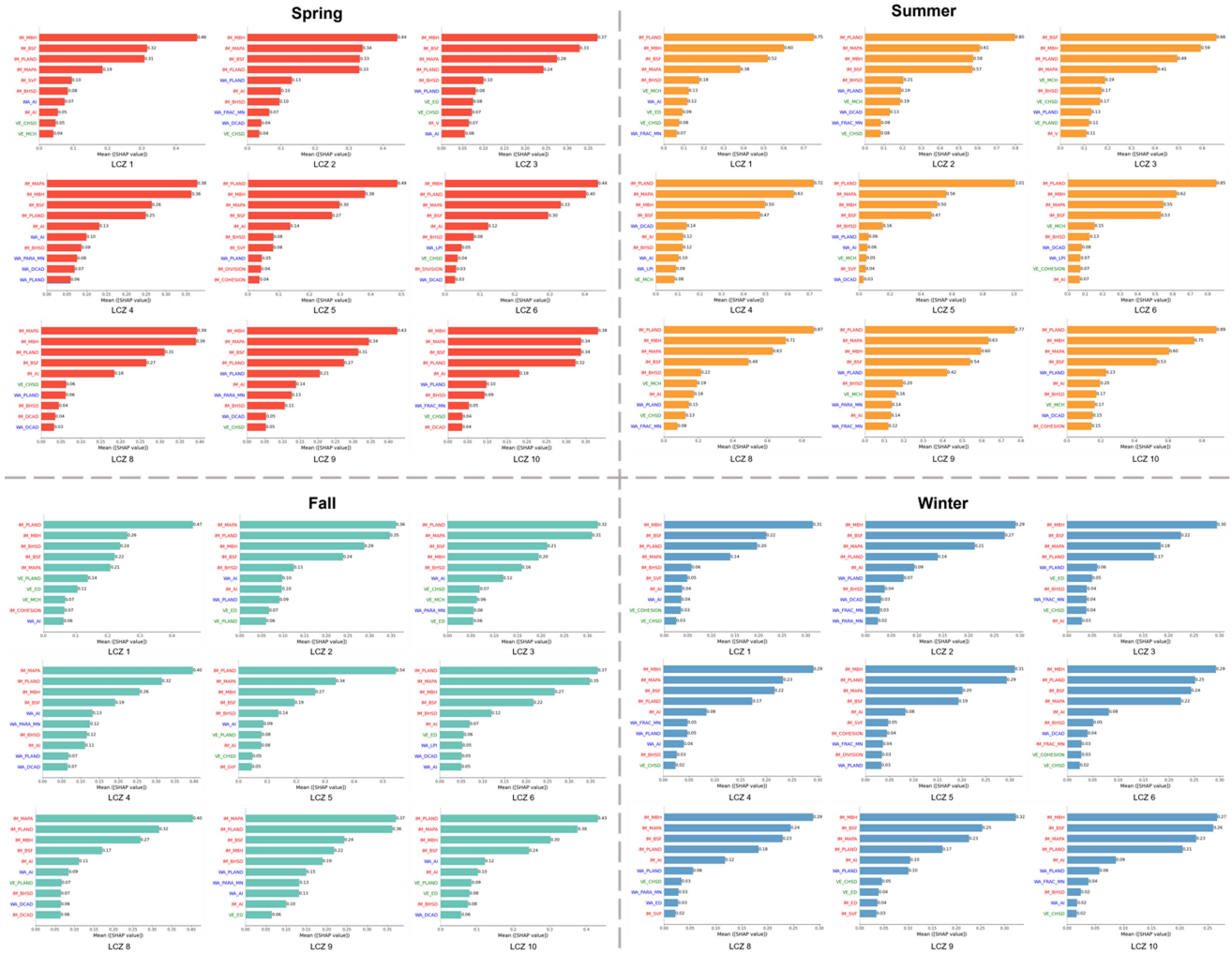

Fig. 5. Relative contribution of metrics on LST in different LCZs across four seasons. The results for spring, summer, fall, and winter are presented as bars in red, yellow, green, and blue, respectively. The morphological indicators of impervious surfaces, vegetation, and water bodies are highlighted in red, green, and blue fonts, respectively.

across seasons, with generally higher interaction effects observed in summer, indicating that the interaction differs seasonally and is significant during the summer. Additionally, variations in the interaction of the same metric pairs across different LCZs suggest that these interactions also differ among LCZ types.

Regarding the interaction between IM_MBH and WA_PLAND, if IM_MBH is below 18 m and WA_PLAND exceeds 15%, WA_PLAND tends to weaken the warming effect of IM_MBH on LST. Conversely, when IM_MBH exceeds 18 m and WA_PLAND is greater than 15%, WA_PLAND enhances the cooling effect of IM_MBH on LST, particularly prominent in LCZ 3 [see Fig. VII in Supplementary and Fig. 8(a)]. However, in LCZ 9 during spring, fall, and winter, when IM_MBH is above 18 m and WA_PLAND exceeds 15%, WA_PLAND instead diminishes the cooling effect of IM_MBH [see Fig. 8(b) and Fig. VII in Supplementary].

The interaction between WA_PLAND and VE_DCAD shows significant seasonal and LCZ-type variability. This interaction is particularly prominent in LCZ 3 during spring, summer, and winter [see Fig. VIII in Supplementary and Fig. 8(c) and (d)]. Specifically, when WA_PLAND is less than 5%, higher values of VE_DCAD (VE_DCAD $>$ 180) tend to suppress the warming effect of WA_PLAND on LST. Conversely, when WA_PLAND exceeds 5%, higher VE_DCAD (VE_DCAD $>$ 180) enhances the effect of WA_PLAND, further strengthening its cooling impact on LST.

V. Discussion

A. Relationship Between Urban Morphology and LST

This study employed the XGBoost and SHAP methods to systematically evaluate the influence of various urban morphology metrics on LST. The results demonstrate that impervious surfaces, vegetation, and water bodies all exert significant effects across different seasons and LCZ types. Among them, impervious surface-related metrics (such as IM_PLAND, IM_MAPA, and IM_BSF) consistently rank high in SHAP values, highlighting their prominent warming effects. IM_PLAND shows a significant positive correlation with LST, which is primarily

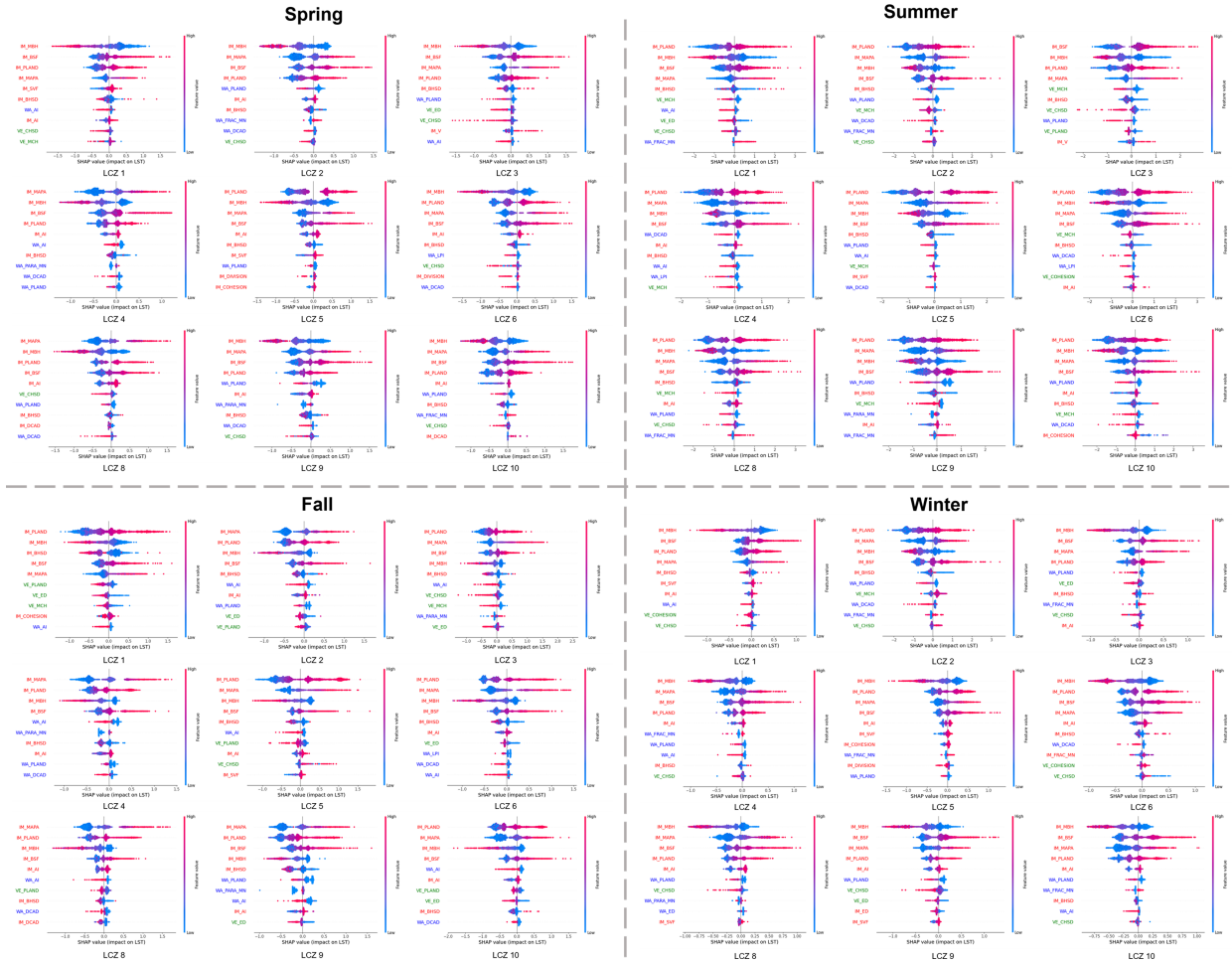

Fig. 6. Global interpretation of metrics on LST in different LCZs across four seasons. The morphological indicators of impervious surfaces, vegetation, and water bodies are highlighted in red, green, and blue fonts, respectively.

attributed to impervious surfaces being composed of materials with high heat capacity and low reflectivity—such as steel, cement, and asphalt—that readily absorb and store solar radiation [69]. This finding is consistent with the results of [70].

Besides, IM_MBH exhibits a certain cooling effect in several LCZ types. This result suggests that when the average building height exceeds 18 m, the resulting shading effect effectively reduces surface radiation absorption and enhances vertical ventilation. These processes facilitate heat dispersion and release, producing a cooling effect [72]. Especially, in Changsha, the high solar altitude angle during summer further implies that only sufficiently tall buildings can generate extensive shadows, which explains why the cooling effect becomes evident only beyond this height threshold. This finding contrasts with the results of [71] that high-rise buildings tend to show stronger urban heat island effects. This discrepancy may arise because the research presented in [71] focused solely on building height, whereas high-rise areas in their study also coincided with higher building density and lower vegetation and water coverage in the study area core, both of which exacerbate heat accumulation and restrict dissipation, thereby strengthening the observed heat island effect.

In addition, to further investigate the shading effect of high-rise buildings, we conducted a regression analysis of IM_MBH, IM_PLAND, VE_PLAND, and LST within high-rise building areas (IM_MBH $>$ 18 m). All three variables exert significant influences on LST, collectively explaining 34.2% of its total variance. Among these predictors, IM_MBH is the most important factor for predicting LST, as indicated by the standardized regression coefficients (see Supplementary Table II). This finding suggests that, in high-rise building areas, the shading effect associated with building height outweighs the heat accumulation effect caused by building density, thereby effectively reducing LST.

Previous studies have shown that green spaces effectively mitigate UHI effects through processes such as evapotranspiration, shading, and photosynthesis [73], [74]. In this study, vegetation morphology metrics (such as VE_CHSD, VE_MCH, and VE_ED) exhibit higher SHAP values during summer, indicating a significant cooling effect of vegetation on LST during periods of active transpiration. Besides, our findings align with those of [37] and [75], demonstrating that increased vegetation cover, particularly in summer, significantly reduces LST. Moreover, VE_MCH plays a critical role in regulating LST.

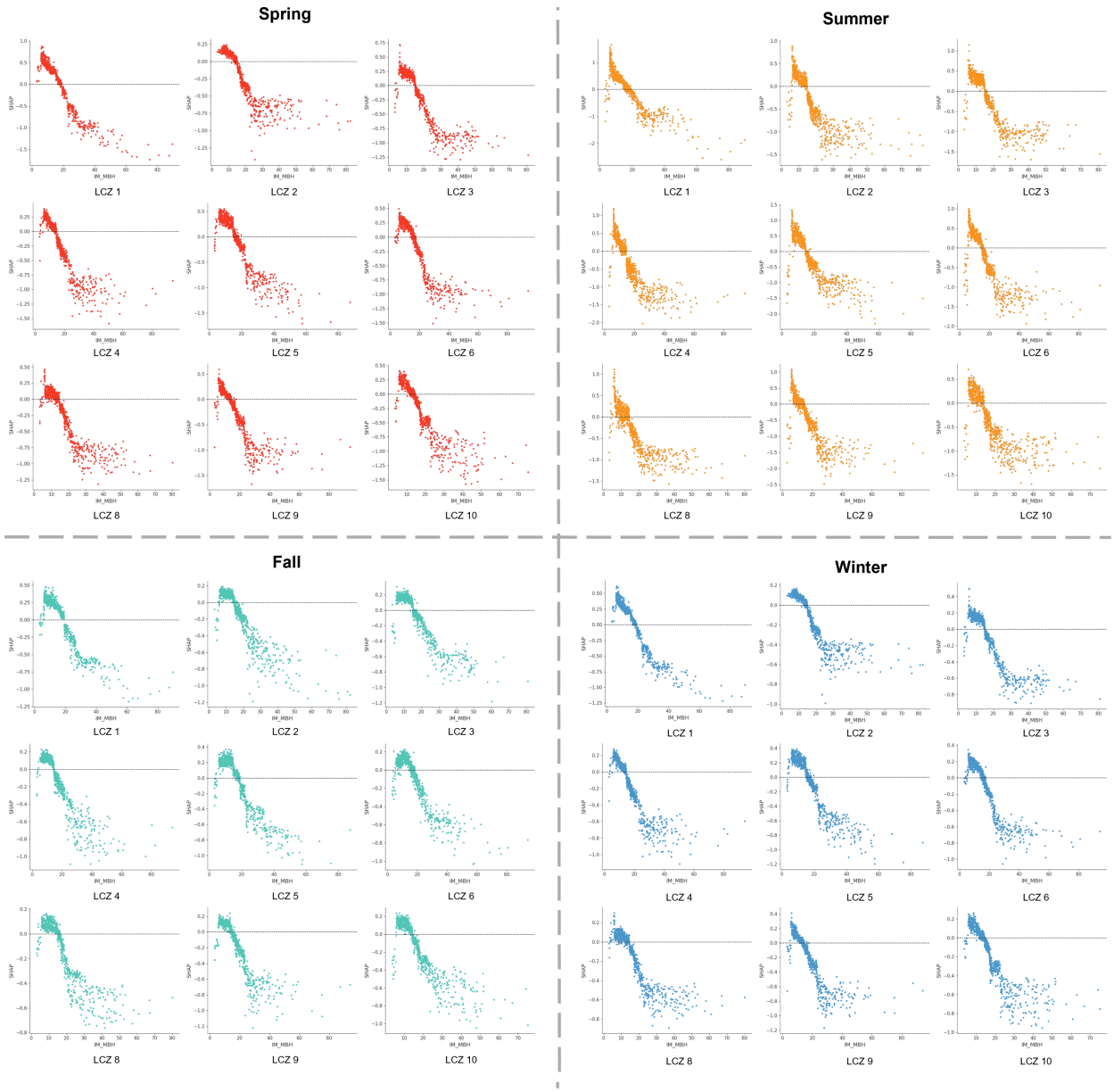

Fig. 7. Marginal effect of IM_MBH on LST in different LCZs across four seasons. The results for spring, summer, fall, and winter are presented as scatterplots in red, yellow, green, and blue, respectively.

Taller vegetation enhances air convection, disrupting the near-surface stagnant layer and accelerating heat exchange with the atmosphere [76], thereby facilitating the transfer of heat to higher atmospheric levels and reducing surface heat accumulation. This study also finds that when VE_MCH is below 3 m, there is still a slight warming effect on LST, likely because low-height vegetation, such as lawns and shrubs, has sparse canopies, limited transpiration, and weak shading capacity. However, when VE_MCH exceeds 3 m, vegetation forms more effective 3-D shading and cooling airflow channels, significantly enhancing the cooling effect [77].

In winter, the influence of VE_CHSD on LST is greater than that of VE_MCH. This difference may be attributed to seasonal changes that weaken the shading effect of vegetation, coupled with overall lower heat accumulation during winter, which reduces the convective cooling effect generated by taller vegetation. Under these conditions, moderate heterogeneity in vegetation height (VE_CHSD) can increase surface roughness, thereby enhancing local air flow and creating small vortices and heat exchange pathways that facilitate heat dissipation [78]. However, when VE_CHSD falls within certain value ranges, its capacity to mitigate UHI effects declines markedly. Overall, the regulatory effect of VE_CHSD on UHI during winter is relatively limited.

Water body morphology metrics, such as WA_PLAND and WA_AI, demonstrate the cooling effect on LST, particularly prominent during the summer. This is likely due to the high specific heat capacity of water, its evaporative cooling potential,

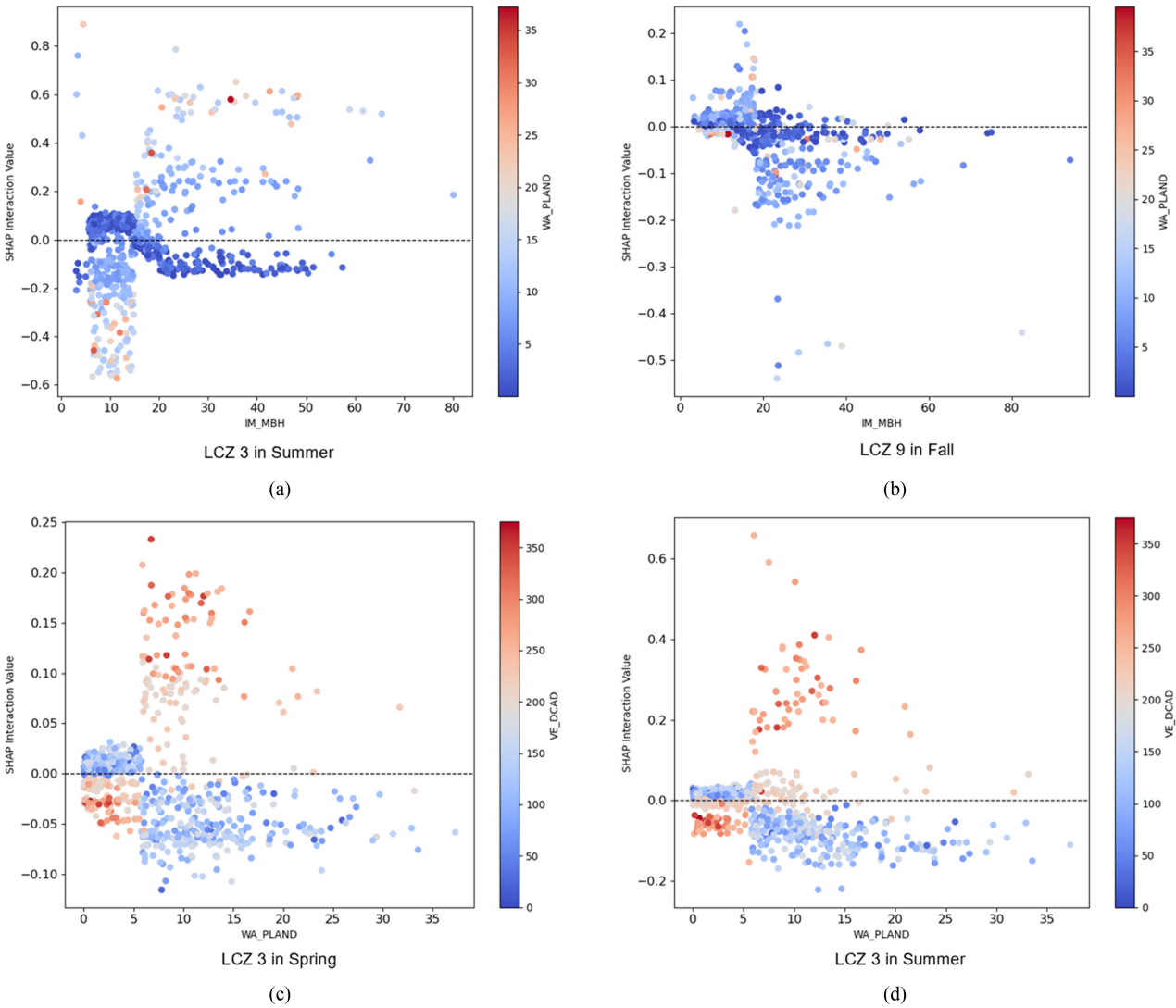

Fig. 8. Key interactive effect of metrics on LST in different LCZs and seasons. (a) Interactive effect between IM_MBH and WA_PLAND of LCZ 3 in summer. (b) Interactive effect between IM_MBH and WA_PLAND of LCZ 9 in fall. (c) Interactive effect between WA_PLAND and VE_DCAD of LCZ 3 in spring. (d) Interactive effect between WA_PLAND and VE_DCAD of LCZ 3 in summer.

and its role in regulating the local microclimate [79]. The cooling effect associated with WA_AI suggests that aggregated water bodies are more effective at reducing temperatures compared to dispersed ones, which aligns with the findings of [80].

B. Complex Interaction Effects of Urban Morphology on LST

Through the analysis of SHAP interaction values, this study reveals the complex interplay among impervious surfaces, vegetation, and water bodies in regulating LST. Specifically, the interaction between building height (IM_MBH) and water body proportion (WA_PLAND) exhibits a nonlinear pattern across most built LCZs. When building heights are relatively low (IM_MBH $<$ 18 m), a higher proportion of water bodies tends to weaken the warming effect of impervious surfaces. Conversely, for taller buildings, the presence of more extensive water bodies may enhance the cooling effect. When the average building height is below 18 m and water coverage exceeds 15%, water bodies effectively mitigate the warming impact of low-rise buildings through evaporative cooling and their high heat capacity. In contrast, when IM_MBH exceeds 18 m and WA_PLAND is greater than 15%, the combined effects of water-induced cooling and shading from taller buildings further amplify the cooling effect in these areas. These findings are consistent with [46], who identified a complex, nonlinear interaction between building height and water body coverage influencing LST. Besides, the interaction between WA_PLAND and vegetation complexity (VE_DCAD) indicates that when water body coverage is low, complex vegetation structures may diminish the overall thermal regulation capacity. However, beyond a certain threshold of water coverage, intricate vegetation patterns synergize with water bodies to further strengthen cooling effects.

C. Seasonal Differences of Urban Morphology Effects on LST

This study found that the impact of urban morphological metrics on LST exhibits a significant seasonal difference, with the strongest effects observed in summer. SHAP value analysis reveals that the explanatory power of various morphological metrics on LST is notably enhanced during summer, indicating that LST is more sensitive to urban morphology in this season. On one hand, the higher solar elevation angle in summer leads to increased radiation intensity [9], and the absorption effect of impervious surfaces on strong solar radiation significantly exacerbates the rise in LST [81]. On the other hand, anthropogenic heat sources, such as air conditioning release, are concentrated in summer, further intensifying the thermal load [82]. Therefore, impervious surface-related metrics (e.g., IM_PLAND) show high SHAP values in summer, reflecting a prominent warming effect. Meanwhile, stronger evapotranspiration conditions in summer enhance the cooling capacity of vegetation and water bodies, making their cooling effects on LST more prominent. In contrast, the overall effect of urban morphology on LST weakens in winter due to reduced radiation and sparse vegetation, consistent with the findings of [83]. Additionally, the influence of IM_MBH on LST is relatively stronger in winter, which may be attributed to the extensive shading effect caused by building height. Due to the lower solar elevation angle in winter, tall buildings are more likely to block sunlight, enhancing surface shading and cooling effects [84]. At the same time, stronger winds and drier air in winter further promote heat exchange between the surface and the atmosphere, accelerating the surface cooling process.

D. Implications for UHI Adaptation Planning in Different LCZs

Based on the findings in this study, urban planning and management strategies should account for unique driving mechanisms across different LCZs to effectively mitigate the UHI effect. In building-dominated areas such as LCZ 1, LCZ 2, and LCZ 3, where impervious surface coverage is high and significant heat accumulation tends to occur, the average building height (IM_MBH) exhibits a clear nonlinear impact on LST. Therefore, increasing building heights beyond critical thresholds (e.g., above 18 m) is recommended to create effective shading and enhance vertical ventilation, thereby alleviating heat island effects. Moreover, optimizing the spatial configuration of water bodies by increasing water body coverage (WA_PLAND) to over 15% can leverage their evaporative cooling potential and synergize with high-density buildings for improved thermal comfort. To further enhance the efficiency of green space utilization, widespread adoption of rooftop greening and vertical greening is encouraged. This approach increases canopy height (VE_MCH) and strengthens shading and evapotranspiration functions, providing multilayered thermal regulation in building-dominated zones.

In open low-density building zones (LCZ 4, LCZ 5, and LCZ 6), the extensive presence of impervious surfaces combined with relatively low building heights (IM_MBH) leads to significant surface heat accumulation, whereas the cooling potential of water bodies remains underutilized. To mitigate these effects, it is advisable to control the impervious surface proportion (IM_PLAND) below a critical threshold (60%) to reduce heat buildup and limit increases in LST. Priority should be given to planning patchy water bodies and increasing overall water body coverage (WA_PLAND) to harness their strong evaporative cooling capacity, thereby alleviating local thermal stress. Simultaneously, introducing tall vegetation with canopy heights exceeding 3 m (VE_MCH $>$ 3m) can enhance shading and evapotranspiration effects. This vegetation also improves air circulation and local microclimate conditions, synergistically boosting the urban thermal environment's resilience in these zones.

In mixed-use urban zones (LCZ 8, LCZ 9, and LCZ 10), the spatial morphology is complex, and the interactions among various factors are significant. SHAP analysis indicates that the combined effects of multiple factors strongly influence LST. Therefore, it is crucial to emphasize synergistic design strategies. For instance, within areas of high average building height (IM_MBH), strategically configuring concentrated water bodies with coverage exceeding 15% (WA_PLAND $>$ 15%) can enhance the combined cooling effects. Simultaneously, maintaining a balanced ratio between impervious surfaces and green spaces is important to prevent excessive expansion of impervious areas (IM_PLAND). Improving vertical greenery (increasing VE_MCH) and enhancing water body connectivity (WA_AI) are recommended to maximize the integrated benefits of green-blue infrastructure. Additionally, increasing vegetation spatial heterogeneity (e.g., by raising VE_CHSD values) can introduce more microclimatic perturbations and pathways for heat exchange, thereby strengthening the area's intrinsic capacity for thermal regulation.

In areas close to existing water bodies or where water landscape elements are planned, it is essential to reasonably increase the proportion of water coverage (WA_PLAND) and enhance the aggregation of water bodies (WA_AI). Avoid excessive fragmentation of water features, as this can weaken their evaporative cooling capacity and microclimate regulation functions. Particularly in densely built-up zones, the synergistic configuration of water bodies and high-rise buildings can significantly amplify cooling effects. Urban planners should leverage this interaction to maximize the benefits of water elements in mitigating urban heat.

E. Limitations and Perspectives

Although this study systematically analyzed the multidimensional impacts of urban morphology on LST, several limitations remain. First, the research focused solely on the influence of urban morphology on LST within the local thermal environment, without considering the vertical temperature situation. While LST reflects surface thermal conditions, it cannot directly measure heat fluxes, which are jointly affected by radiation, conduction, convection, and the heat storage capacity of the surface. Therefore, future studies will incorporate air temperature and other environmental variables to achieve a more comprehensive understanding of how urban morphology affects heat flux dynamics. This would provide a stronger scientific foundation for developing systematic and effective urban cooling strategies.

Second, this study used a representative area in Changsha to analyze the impact of urban morphology on LST. However, the interactions among urban morphology characteristics may vary heterogeneously across different geographic settings due to differences in climate and socioeconomic development levels. Therefore, future studies will extend this research to cities with diverse urbanization patterns and climatic conditions. It would not only deepen the understanding of the critical role of morphological interactions in mitigating LST but also help assess the generalizability and applicability of the methods and findings presented here.

Third, the vegetation canopy height data used in this study were derived from 2020, whereas LST and land cover data were obtained in 2022. This temporal mismatch may introduce some uncertainty into the analysis of the relationship between vegetation and LST. However, the potential impact is considered limited. This is because large-scale urban reconstruction and land-use changes have mainly occurred at the urban fringe, whereas the study areas, the city center have remained relatively stable during the study period. Moreover, Changsha is dominated by evergreen broad-leaved forests, whose canopy height shows minimal variation over a two-year period.

Finally, future research may apply this framework to diverse urban contexts, account for temporal dynamics in urban development, or integrate broader environmental variables, thereby promoting high-quality and sustainable urban development.

VI. Conclusion

This study focuses on the driving mechanisms of LST in urban areas. It systematically investigates how three types of urban elements—impervious surfaces, vegetation, and water bodies—affect LST across different LCZs and seasons. By capturing both the direct effects and interaction patterns of these key urban elements at a fine spatial scale, the study offers new theoretical insights into the formation of urban thermal environments. The key findings can be summarized in the following three main aspects.

1) At a 200-m scale, morphology metrics have the greatest explanatory power on LST.
2) Urban morphology's impact on LST exhibits significant differences across LCZs and seasons. Most impervious surface metrics (e.g., IM_PLAND, IM_MAPA, and IM_BSF) generally act as dominant warming drivers, whereas vegetation and water body factors (e.g., VE_MCH and WA_PLAND) consistently demonstrate cooling effects.
3) Significant interactions exist between IM_MBH and WA_PLAND, as well as between WA_PLAND and VE_DCAD.

These findings lay a solid foundation for studying urban thermal effects and help advance climate-responsive design and more effective heat mitigation strategies.

References

[1] T. R. Oke, "The energetic basis of the urban heat island," *Quart. J. Roy. Meteorol. Soc.*, vol. 108, no. 455, pp. 1–24, 1982.

[2] E. Kalisa, S. Fadlallah, M. Amani, L. Nahayo, and G. Habiyaremye, "Temperature and air pollution relationship during heatwaves in Birmingham, U.K.," *Sustain. Cities Soc.*, vol. 43, pp. 111–120, Nov. 2018, doi: 10.1016/j.scs.2018.08.033.

[3] A. Azhdari, A. Soltani, and M. Alidadi, "Urban morphology and landscape structure effect on land surface temperature: Evidence from Shiraz, a semi-arid city," *Sustain. Cities Soc.*, vol. 41, pp. 853–864, Aug. 2018, doi: 10.1016/j.scs.2018.06.034.

[4] G. Grigoraș and B. Urițescu, "Land use/land cover changes dynamics and their effects on surface urban heat island in Bucharest, Romania," *Int. J. Appl. Earth Observ. Geoinf.*, vol. 80, pp. 115–126, Aug. 2019, doi: 10.1016/j.jag.2019.03.009.

[5] Q. Liu, T. Hang, and Y. Wu, "Unveiling differential impacts of multidimensional urban morphology on heat island effect across local climate zones: Interpretable CatBoost-SHAP machine learning model," *Building Environ.*, vol. 270, Feb. 2025, Art. no. 112574, doi: 10.1016/j.buildenv.2025.112574.

[6] B. Yuan, L. Zhou, F. Hu, and C. Wei, "Effects of 2D/3D urban morphology on land surface temperature: Contribution, response, and interaction," *Urban Climate*, vol. 53, Jan. 2024, Art. no. 101791, doi: 10.1016/j.uclim.2023.101791.

[7] M. Zhou, R. Wang, and Y. Guo, "How urban spatial characteristics impact surface urban heat island in subtropical high-density cities based on LCZs: A case study of Macau," *Sustain. Cities Soc.*, vol. 112, Oct. 2024, Art. no. 105587, doi: 10.1016/j.scs.2024.105587.

[8] F. Yuan and M. E. Bauer, "Comparison of impervious surface area and normalized difference vegetation index as indicators of surface urban heat island effects in Landsat imagery," *Remote Sens. Environ.*, vol. 106, no. 3, pp. 375–386, Feb. 2007, doi: 10.1016/j.rse.2006.09.003.

[9] C. Berger, J. Rosentreter, M. Voltersen, C. Baumgart, C. Schmullius, and S. Hese, "Spatio-temporal analysis of the relationship between 2D/3D urban site characteristics and land surface temperature," *Remote Sens. Environ.*, vol. 193, pp. 225–243, May 2017, doi: 10.1016/j.rse.2017.02.020.

[10] J. Li, X. Wang, X. Wang, W. Ma, and H. Zhang, "Remote sensing evaluation of urban heat island and its spatial pattern of the Shanghai metropolitan area, China," *Ecol. Complexity*, vol. 6, no. 4, pp. 413–420, Dec. 2009, doi: 10.1016/j.ecocom.2009.02.002.

[11] J. He, Y. Shi, L. Xu, Z. Lu, and M. Feng, "An investigation on the impact of blue and green spatial pattern alterations on the urban thermal environment: A case study of Shanghai," *Ecol. Indicators*, vol. 158, Jan. 2024, Art. no. 111244, doi: 10.1016/j.ecolind.2023.111244.

[12] Y. Gao, J. Zhao, and K. Yu, "Effects of block morphology on the surface thermal environment and the corresponding planning strategy using the geographically weighted regression model," *Building Environ.*, vol. 216, May 2022, Art. no. 109037, doi: 10.1016/j.buildenv.2022.109037.

[13] P. Zeng et al., "The influence of the landscape pattern on the urban land surface temperature varies with the ratio of land components: Insights from 2D/3D building/vegetation metrics," *Sustain. Cities Soc.*, vol. 78, Mar. 2022, Art. no. 103599, doi: 10.1016/j.scs.2021.103599.

[14] R. C. Estoque, Y. Murayama, and S. W. Myint, "Effects of landscape composition and pattern on land surface temperature: An urban heat island study in the megacities of Southeast Asia," *Sci. Total Environ.*, vol. 577, pp. 349–359, Jan. 2017, doi: 10.1016/j.scitotenv.2016.10.195.

[15] X. Huang and Y. Wang, "Investigating the effects of 3D urban morphology on the surface urban heat island effect in urban functional zones by using high-resolution remote sensing data: A case study of Wuhan, Central China," *ISPRS J. Photogrammetry Remote Sens.*, vol. 152, pp. 119–131, Jun. 2019, doi: 10.1016/j.isprsjprs.2019.04.010.

[16] Z. Cai, Y. Tang, L. Chang, and M. Demuzere, "Analyzing the transformation of 3D urban morphology and corresponding surface heat island effect in Beijing," *Urban Plan. Int.*, vol. 36, no. 5, 2021, Art. no. 5, doi: 10.19830/j.upi.2021.407.

[17] R. Ellefsen, "Mapping and measuring buildings in the canopy boundary layer in ten U.S. cities," *Energy Buildings*, vol. 16, no. 3, pp. 1025–1049, Jan. 1991, doi: 10.1016/0378-7788(91)90097-M.

[18] T. R. Oke, *Initial Guidance to Obtain Representative Meteorological Observations At Urban Sites*, vol. 81. Geneva, Switzerland: World Meteorol. Org., 2004.

[19] C. Yang et al., "Assessing the effects of 2D/3D urban morphology on the 3D urban thermal environment by using multi-source remote sensing data and UAV measurements: A case study of the snow-climate city of Changchun, China," *J. Cleaner Prod.*, vol. 321, Oct. 2021, Art. no. 128956, doi: 10.1016/j.jclepro.2021.128956.

[20] I. D. Stewart and T. R. Oke, "Local climate zones for urban temperature studies," *Bull. Amer. Meteorol. Soc.*, vol. 93, no. 12, pp. 1879–1900, Dec. 2012, doi: 10.1175/BAMS-D-11-00019.1.

[21] R. Wang, M. Cai, C. Ren, B. Bechtel, Y. Xu, and E. Ng, "Detecting multi-temporal land cover change and land surface temperature in Pearl River Delta by adopting local climate zone," *Urban Climate*, vol. 28, Jun. 2019, Art. no. 100455, doi: 10.1016/j.uclim.2019.100455.

[22] B. Yuan et al., "Global distinct variations of surface urban heat islands in inter- and intra-cities revealed by local climate zones and seamless daily land surface temperature data," *ISPRS J. Photogrammetry Remote Sens.*, vol. 204, pp. 1–14, Oct. 2023, doi: 10.1016/j.isprsjprs.2023.08.012.

[23] Y. Chen, B. Zheng, and Y. Hu, "Mapping local climate zones using ArcGIS-based method and exploring land surface temperature characteristics in Chenzhou, China," *Sustainability*, vol. 12, no. 7, Jan. 2020, Art. no. 7, doi: 10.3390/su12072974.

[24] P. Du, J. Chen, X. Bai, and W. Han, "Understanding the seasonal variations of land surface temperature in Nanjing urban area based on local climate zone," *Urban Climate*, vol. 33, Sep. 2020, Art. no. 100657, doi: 10.1016/j.uclim.2020.100657.

[25] J. Geletič, M. Lehnert, and P. Dobrovolný, "Land surface temperature differences within local climate zones, based on two central European cities," *Remote Sens.*, vol. 8, no. 10, Oct. 2016, Art. no. 10, doi: 10.3390/rs8100788.

[26] A. Zwolska, M. Półrolniczak, and L. Kolendowicz, "Urban growth's implications on land surface temperature in a medium-sized European city based on LCZ classification," *Sci. Rep.*, vol. 14, no. 1, Apr. 2024, Art. no. 8308, doi: 10.1038/s41598-024-58501-0.

[27] P. Y. Fan et al., "Spatially-heterogeneous impacts of surface characteristics on urban thermal environment, a case of the Guangdong-Hong Kong-Macau Greater Bay Area," *Urban Climate*, vol. 41, Jan. 2022, Art. no. 101034, doi: 10.1016/j.uclim.2021.101034.

[28] C. Hong et al., "Vertical thermal environment investigation in different urban zones (LCZ4/LCZ6/LCZA) and heat mitigation evaluation: Field measurements and numerical simulations," *Building Environ.*, vol. 262, Aug. 2024, Art. no. 111840, doi: 10.1016/j.buildenv.2024.111840.

[29] P. Bansal and S. J. Quan, "Relationships between building characteristics, urban form and building energy use in different local climate zone contexts: An empirical study in Seoul," *Energy Buildings*, vol. 272, Oct. 2022, Art. no. 112335, doi: 10.1016/j.enbuild.2022.112335.

[30] J. Chen et al., "Quantifying the main and interactive effects of the dominant factors on the diurnal cycles of land surface temperature in typical urban functional zones," *Sustain. Cities Soc.*, vol. 114, Nov. 2024, Art. no. 105727, doi: 10.1016/j.scs.2024.105727.

[31] V. Kirschner, K. Macků, D. Moravec, and J. Maňas, "Measuring the relationships between various urban green spaces and local climate zones," *Sci. Rep.*, vol. 13, no. 1, Jun. 2023, Art. no. 9799, doi: 10.1038/s41598-023-36850-6.

[32] R. Wang and M. Wang, "Multi-scale analysis of surface thermal environment in relation to urban form: A case study of the Guangdong-Hong Kong-Macao Greater Bay Area," *Sustain. Cities Soc.*, vol. 99, Dec. 2023, Art. no. 104953, doi: 10.1016/j.scs.2023.104953.

[33] Y. Feng, G. Wu, S. Ge, F. Feng, and P. Li, "Identification of key drivers of land surface temperature within the local climate zone framework," *Land*, vol. 14, no. 4, Apr. 2025, Art. no. 771, doi: 10.3390/land14040771.

[34] Ş.-C. Creţu, L. Sfîcă, P. Ichim, V.-A. Amihăesei, I.-G. Breabăn, and L. Roşu, "Warm season land surface temperature and its relationship with local climate zones in post-socialist cities," *Theor. Appl. Climatol.*, vol. 156, no. 4, Mar. 2025, Art. no. 191, doi: 10.1007/s00704-025-05409-y.

[35] R. Olgun et al., "Impacts of landscape composition on land surface temperature in expanding desert cities: A case study in Arizona, USA," *Land*, vol. 14, no. 6, Jun. 2025, Art. no. 1274, doi: 10.3390/land14061274.

[36] A. Zwolska, M. Półrolniczak, and L. Kolendowicz, "Urban growth's implications on land surface temperature in a medium-sized European city based on LCZ classification," *Sci. Rep.*, vol. 14, no. 1, Apr. 2024, Art. no. 8308, doi: 10.1038/s41598-024-58501-0.

[37] L. Lin, Y. Zhao, J. Zhao, and D. Wang, "Comprehensively assessing seasonal variations in the impact of urban greenspace morphology on urban heat island effects: A multidimensional analysis," *Sustain. Cities Soc.*, vol. 118, Jan. 2025, Art. no. 106014, doi: 10.1016/j.scs.2024.106014.

[38] Y. Lu, W. Yue, Y. Liu, and Y. Huang, "Investigating the spatiotemporal non-stationary relationships between urban spatial form and land surface temperature: A case study of Wuhan, China," *Sustain. Cities Soc.*, vol. 72, Sep. 2021, Art. no. 103070, doi: 10.1016/j.scs.2021.103070.

[39] W. Zhou, G. Huang, and M. L. Cadenasso, "Does spatial configuration matter? Understanding the effects of land cover pattern on land surface temperature in urban landscapes," *Landscape Urban Plan.*, vol. 102, no. 1, pp. 54–63, Jul. 2011, doi: 10.1016/j.landurbplan.2011.03.009.

[40] B. Chun and J.-M. Guldmann, "Impact of greening on the urban heat island: Seasonal variations and mitigation strategies," *Comput., Environ. Urban Syst.*, vol. 71, pp. 165–176, Sep. 2018, doi: 10.1016/j.compenvurbsys.2018.05.006.

[41] W. Zhao, S.-B. Duan, A. Li, and G. Yin, "A practical method for reducing terrain effect on land surface temperature using random forest regression," *Remote Sens. Environ.*, vol. 221, pp. 635–649, Feb. 2019, doi: 10.1016/j.rse.2018.12.008.

[42] D. Hu et al., "How do urban morphological blocks shape spatial patterns of land surface temperature over different seasons? A multifactorial driving analysis of Beijing, China," *Int. J. Appl. Earth Observ. Geoinf.*, vol. 106, Feb. 2022, Art. no. 102648, doi: 10.1016/j.jag.2021.102648.

[43] L. Zhou, F. Hu, B. Wang, C. Wei, D. Sun, and S. Wang, "Relationship between urban landscape structure and land surface temperature: Spatial hierarchy and interaction effects," *Sustain. Cities Soc.*, vol. 80, May 2022, Art. no. 103795, doi: 10.1016/j.scs.2022.103795.

[44] R. Guo et al., "Machine learning-based prediction of outdoor thermal comfort: Combining Bayesian optimization and the SHAP model," *Building Environ.*, vol. 254, 2024, Art. no. 111301, doi: 10.1016/j.buildenv.2024.111301.

[45] S. M. Lundberg and S.-I. Lee, "A unified approach to interpreting model predictions," *Proc. 31st Int. Conf. Neural Inf. Process. Syst.*, 2017, vol. 30, pp. 4768–4777. [Online]. Available: https://proceedings.neurips.cc/paper/2017/hash/8a20a8621978632d76c43dfd28b67767-Abstract.html, Accessed: May 7, 2025.

[46] Y. Xiang et al., "Seasonal variations of the relationship between spectral indexes and land surface temperature based on local climate zones: A study in three Yangtze River megacities," *Remote Sens.*, vol. 15, no. 4, Jan. 2023, Art. no. 4, doi: 10.3390/rs15040870.

[47] H. Xu, F. Sun, P. Zeng, X. Bao, and Y. Che, "Impact of diurnal variation in 3D urban landscape metrics on land surface temperature in Shanghai: A local climate zone perspective," *Energy Buildings*, vol. 336, 2025, Art. no. 115624, doi: 10.1016/j.enbuild.2025.115624.

[48] M. Ge et al., "Research on thermal environment influencing mechanism and cooling model based on local climate zones: A case study of the Changsha–Zhuzhou–Xiangtan urban agglomeration," *Remote Sens.*, vol. 17, no. 14, 2025, Art. no. 2391, doi: 10.3390/rs17142391.

[49] G. Pappaccogli, A. Esposito, and R. Buccolieri, "Summer diurnal LST variability across local climate zones using ECOSTRESS data in Lecce and Milan," *Atmosphere*, vol. 16, no. 4, 2025. Art. no. 4, doi: 10.3390/atmos16040377.

[50] N. Lang, W. Jetz, K. Schindler, and J. D. Wegner, "A high-resolution canopy height model of the Earth," *Nature Ecol. Evol.*, vol. 7, no. 11, pp. 1778–1789, 2023, doi: 10.1038/s41559-023-02206-6.

[51] P. Luo et al., "Identifying determinants of spatio-temporal disparities in soil moisture of the Northern Hemisphere using a geographically optimal zones-based heterogeneity model," *ISPRS J. Photogrammetry Remote Sens.*, vol. 185, pp. 111–128, Mar. 2022, doi: 10.1016/j.isprsjprs.2022.01.009.

[52] K. McGarigal, S. A. Cushman, and E. Ene, "FRAGSTATS v4: Spatial Pattern Analysis Program for Categorical Maps," Computer software program produced by the authors. [Online]. Available: https://www.fragstats.org, 2023.

[53] O. Conrad et al., "System for automated geoscientific analyses (SAGA) v. 2.1. 4," *Geosci. Model Develop.*, vol. 8, no. 7, pp. 1991–2007, 2015, doi: 10.5194/gmd-8-1991-2015.

[54] J. Song, S. Du, X. Feng, and L. Guo, "The relationships between landscape compositions and land surface temperature: Quantifying their resolution sensitivity with spatial regression models," *Landscape Urban Plan.*, vol. 123, pp. 145–157, Mar. 2014, doi: 10.1016/j.landurbplan.2013.11.014.

[55] M. Masoudi and P. Y. Tan, "Multi-year comparison of the effects of spatial pattern of urban green spaces on urban land surface temperature," *Landscape Urban Plan.*, vol. 184, pp. 44–58, Apr. 2019, doi: 10.1016/j.landurbplan.2018.10.023.

[56] Y. Zhang, Y. Wang, and N. Ding, "Spatial effects of landscape patterns of urban patches with different vegetation fractions on urban thermal environment," *Remote Sens.*, vol. 14, no. 22, Nov. 2022, Art. no. 22, doi: 10.3390/rs14225684.

[57] W. Yu et al., "Downscaling mapping method for local climate zones from the perspective of deep learning," *Urban Climate*, vol. 49, May 2023, Art. no. 101500, doi: 10.1016/j.uclim.2023.101500.
[58] Y. Song, J. Wang, Y. Ge, and C. Xu, "An optimal parameters-based geographical detector model enhances geographic characteristics of explanatory variables for spatial heterogeneity analysis: Cases with different types of spatial data," *GIScience Remote Sens.*, vol. 57, no. 5, pp. 593–610, Jul. 2020, doi: 10.1080/15481603.2020.1760434.
[59] X. X. Zhu et al., "So2Sat LCZ42: A benchmark data set for the classification of global local climate zones [Software and Data Sets]," *IEEE Geosci. Remote Sens. Mag.*, vol. 8, no. 3, pp. 76–89, Sep. 2020, doi: 10.1109/MGRS.2020.2964708.
[60] X.-Y. Tong et al., "Land-cover classification with high-resolution remote sensing images using transferable deep models," *Remote Sens. Environ.*, vol. 237, Feb. 2020, Art. no. 111322, doi: 10.1016/j.rse.2019.111322.
[61] Y. Zheng et al., "GIS-based mapping of Local Climate Zone in the high-density city of Hong Kong," *Urban Climate*, vol. 24, pp. 419–448, Jun. 2018, doi: 10.1016/j.uclim.2017.05.008.
[62] K. He, X. Zhang, S. Ren, and J. Sun, "Deep residual learning for image recognition," in *Proc. IEEE Conf. Comput. Vis. Pattern Recognit.*, 2016, pp. 770–778. doi: 10.1109/cvpr.2016.90.
[63] F. Huang et al., "Mapping local climate zones for cities: A large review," *Remote Sens. Environ.*, vol. 292, 2023, Art. no. 113573, doi: 10.1016/j.rse.2023.113573.
[64] B. Bechtel et al., "Quality of crowdsourced data on urban morphology—The human influence experiment (HUMINEX)," *Urban Sci.*, vol. 1, no. 2, Jun. 2017, Art. no. 2, doi: 10.3390/urbansci1020015.
[65] Z. Chen et al., "Delineating seasonal relationships between Suomi NPP-VIIRS nighttime light and human activity across Shanghai, China," *IEEE J. Sel. Topics Appl. Earth Observ. Remote Sens.*, vol. 12, no. 11, pp. 4275–4283, Nov. 2019, doi: 10.1109/JSTARS.2019.2916323.
[66] B. Wu et al., "The relationship between urban 2-D/3-D landscape pattern and nighttime light intensity," *IEEE J. Sel. Topics Appl. Earth Observ. Remote Sens.*, vol. 15, pp. 478–489, 2022, doi: 10.1109/JSTARS.2021.3135488.
[67] L. S. Shapley, "Stochastic games∗," *Proc. Nat. Acad. Sci. USA*, vol. 39, no. 10, pp. 1095–1100, Oct. 1953, doi: 10.1073/pnas.39.10.1095.
[68] M. T. Ribeiro, S. Singh, and C. Guestrin, "Model-agnostic interpretability of machine learning," in *Proc. ICML*, New York, NY, 2016, doi: 10.48550/arXiv.1606.05386.
[69] J. Wang and W. Ouyang, "Attenuating the surface urban heat island within the local thermal zones through land surface modification," *J. Environ. Manage.*, vol. 187, pp. 239–252, Feb. 2017, doi: 10.1016/j.jenvman.2016.11.059.
[70] N. Ding, Y. Zhang, Y. Wang, L. Chen, K. Qin, and X. Yang, "Effect of landscape pattern of urban surface evapotranspiration on land surface temperature," *Urban Climate*, vol. 49, May 2023, Art. no. 101540, doi: 10.1016/j.uclim.2023.101540.
[71] C. Xi, C. Ren, J. Wang, Z. Feng, and S.-J. Cao, "Impacts of urban-scale building height diversity on urban climates: A case study of Nanjing, China," *Energy Buildings*, vol. 251, Nov. 2021, Art. no. 111350, doi: 10.1016/j.enbuild.2021.111350.
[72] Z. Lin, H. Xu, X. Yao, C. Yang, and L. Yang, "Exploring the relationship between thermal environmental factors and land surface temperature of a 'furnace city' based on local climate zones," *Building Environ.*, vol. 243, Sep. 2023, Art. no. 110732, doi: 10.1016/j.buildenv.2023.110732.
[73] P. J. Hardin and R. R. Jensen, "The effect of urban leaf area on summertime urban surface kinetic temperatures: A terre haute case study," *Urban Forestry Urban Greening*, vol. 6, no. 2, pp. 63–72, 2007, doi: 10.1016/j.ufug.2007.01.005.
[74] Z. Liu et al., "Spatialized importance of key factors affecting park cooling intensity based on the park scale," *Sustain. Cities Soc.*, vol. 99, 2023, Art. no. 104952, doi: 10.1016/j.scs.2023.104952.
[75] X. Chen, H. Wang, and J. Yang, "Effect of green blue spaces on the urban thermal environment: A field study in Hong Kong," *Urban Climate*, vol. 55, May 2024, Art. no. 101912, doi: 10.1016/j.uclim.2024.101912.
[76] K. R. Gunawardena, M. J. Wells, and T. Kershaw, "Utilising green and bluespace to mitigate urban heat island intensity," *Sci. Total Environ.*, vol. 584–585, pp. 1040–1055, Apr. 2017, doi: 10.1016/j.scitotenv.2017.01.158.
[77] J. R. Simpson and E. G. McPherson, "Simulation of tree shade impacts on residential energy use for space conditioning in sacramento," *Atmospheric Environ.*, vol. 32, no. 1, pp. 69–74, 1998, doi: 10.1016/S1352-2310(97)00181-7.
[78] A. T. Chan, E. S. So, and S. C. Samad, "Strategic guidelines for street canyon geometry to achieve sustainable street air quality," *Atmos. Environ.*, vol. 35, no. 24, pp. 4089–4098, 2001, doi: 10.1016/S1352-2310(01)00212-6.
[79] P. Ampatzidis and T. Kershaw, "A review of the impact of blue space on the urban microclimate," *Sci. Total Environ.*, vol. 730, Aug. 2020, Art. no. 139068, doi: 10.1016/j.scitotenv.2020.139068.
[80] H. Hou and R. C. Estoque, "Detecting cooling effect of landscape from composition and configuration: An urban heat island study on Hangzhou," *Urban Forestry Urban Greening*, vol. 53, Aug. 2020, Art. no. 126719, doi: 10.1016/j.ufug.2020.126719.
[81] Z. Yu et al., "Enhanced observations from an optimized soil-canopy-photosynthesis and energy flux model revealed evapotranspiration-shading cooling dynamics of urban vegetation during extreme heat," *Remote Sens. Environ.*, vol. 305, 2024, Art. no. 114098, doi: 10.1016/j.rse.2024.114098.
[82] Z. Lin and H. Xu, "Anthropogenic heat flux estimation based on Luojia 1-01 new nighttime light data: A case study of Jiangsu province, China," *Remote Sens.*, vol. 12, no. 22, Jan. 2020, Art. no. 22, doi: 10.3390/rs12223707.
[83] X. Gui, L. Wang, R. Yao, D. Yu, and C. Li, "Investigating the urbanization process and its impact on vegetation change and urban heat island in Wuhan, China," *Environ. Sci. Pollut. Res.*, vol. 26, no. 30, pp. 30808–30825, Oct. 2019, doi: 10.1007/s11356-019-06273-w.
[84] Y. Chen, J. Wu, K. Yu, and D. Wang, "Evaluating the impact of the building density and height on the block surface temperature," *Building Environ.*, vol. 168, 2020, Art. no. 106493, doi: 10.1016/j.buildenv.2019.106493.

Geng Sun received the B.S. degree in geographic information science from Central South University, Changsha, China, in 2021, where he is currently working toward the Ph.D. degree in geomatics science and technology.

His research interests include intelligent interpretation of high-resolution remote sensing images, urban morphology, and urban climate.

Zikun Dong received the M.S. degree in geodesy and geomatics engineering from Central South University, Changsha, China, in 2024.

His research interests include urban heat island, urban morphology, and urban climate.

Meng Cai received her Ph.D. degree in architecture from The Chinese University of Hong Kong, Hong Kong, in 2022, and the B.Eng. degree in geodesy and geomatics engineering from Wuhan University, Wuhan, China, in 2014.

She is currently an Assistant Professor with Wuhan University. Her research interests include the nexus of urban morphology, carbon emissions, and local climate, with particular emphasis on urban renewal, low-carbon pathways, and sustainable urban development.

Ya Guo received the M.S. degree in geodesy and geomatics engineering from the China University of Geosciences (Beijing), Beijing, China, in 2020. He is currently working toward the Ph.D. degree in geomatics science and technology with Central South University, Changsha, China.

His research interests include remote sensing image intelligent interpretation and urban morphology.

Yang Chen received the M.S. degree in technology management and Ph.D. degree in civil and environmental engineering from The Hong Kong Polytechnic University (PolyU), Hong Kong, in 2018 and 2024, respectively.

She is currently a Postdoctoral Fellow with the Department of Civil and Environmental Engineering, PolyU. Her research interests include nature-based solutions, urban ecological conservation, river restoration, and pavement engineering.

Dr. Chen is a reviewer for several journals of urban sustainability.

Jie Chen (Member, IEEE) received the M.S. degree in cartography and geographic information engineering from East China University of Technology, Nanchang, China, in 2006, and the Ph.D. degree in cartography and geographic information engineering from Central South University, Changsha, China, in 2010.

He is currently a Professor with the Department of Geo-Informatics, Central South University. His research interests include intelligent analysis of remote sensing images and urban morphology.

Dr. Chen is a reviewer for several journals in the field of remote sensing.